Section S1. Detailed Methodology

S1.1 The closed-loop integral method

The closed-loop integral method is employed to quantify the NO_2 transport flux across the TP, as defined in Equations (1)-(3). A schematic overview of the procedure is provided in Fig. S1.

$$Flux, in \approx -\sum VCD(S_i) \cdot \omega_i \cdot \cos\beta_i \cdot \Delta S_i \ , \ \beta_i > 90^{\circ} \quad (1)$$

$$Flux, out \approx \sum VCD(S_i) \cdot \omega_i \cdot \cos\beta_i \cdot \Delta S_i \ , \ \beta_i < 90^{\circ} \quad (2)$$

$$Flux, net = Flux, in - Flux, out \quad (3)$$

Here, $VCD(S_i)$ is the NO_2 column along segment S_i, and β_i denotes the angle between the wind vector and the boundary normal vector $\boldsymbol{n}$. $\beta_i > 90^{\circ}$ identifies boundary external influx (import), while $\beta_i < 90^{\circ}$ denotes internal efflux (export). ΔS_i is the boundary integration step. The net flux is calculated as total influx minus efflux, with positive (negative) values indicating net import (export).

S1.2 Regression model for trend analysis

In this study, a unified regression framework was applied to the long-term time series of tropospheric NO_2 column concentrations, surface concentrations, and transport fluxes, in order to capture their secular trends and seasonal cycle characteristics (Yin et al., 2022). The model integrates a linear term with third-order Fourier components, as formulated in Equation (4).

$$Y(t)=A_0+A_1 t+A_2 \cos\left(\frac{2\pi t}{12}\right)+A_3 \sin\left(\frac{2\pi t}{12}\right)+A_4 \cos\left(\frac{4\pi t}{12}\right)+A_5 \sin\left(\frac{4\pi t}{12}\right) \quad (4)$$

The modeled variable $Y(t)$ was decomposed into a linear component representing long-term evolution and harmonic terms describing seasonal variability. The parameters A_0 and A_1 denote the intercept and linear growth rate, respectively, while A_2-A_5 account for the periodic seasonal cycle. The interannual rate of change was estimated as A_1/A_0, with associated uncertainties expressed as mean ± standard deviation.

S1.3 Wind field correction and uncertainty

To reduce vertical non-uniformity errors, we apply a NO_2-weighted vertical wind correction, with wind-field uncertainty quantified using Equations (5)-(7).

$$\tau_j(z_j) = \frac{x_j(z_j) \cdot Airmass_j(z_j)}{\sum_i x_j(z_j) \cdot Airmass_j(z_j)} \quad (5)$$

$$\omega_{j,avg} = \sum_i \omega(z_i) \cdot \tau_j(z_j), \quad \theta_{j,avg} = \sum_i \theta(z_i) \cdot \tau_j(z_j) \quad (6)$$

$$\sigma_{\omega z} = \sqrt{\sum_i [\tau_j(\omega_{j,avg} - \omega(z_i))]^2}, \sigma_{\theta z} = \sqrt{\sum_i [\tau_j(\theta_{j,avg} - \theta(z_i))]^2} \quad (7)$$

Where $\omega(z_i)$, $x_j(z_j)$, and $Airmass_j(z_j)$ represent the wind field vector, NO_2 VMR concentration, and air mass at height z_j along the j segment of the integration path, respectively. $\omega_{j,avg}$ is the weighting averaged wind field along the j segment of the integration path, and $\sigma_{\omega z}$ and $\sigma_{\theta z}$ are the uncertainties in the corrected wind field and wind direction, respectively.

Section S2. Random Forest Hyperparameter Selection and Performance

Each parameter combination was evaluated using the coefficient of determination (R^2), and the configuration with the highest average R^2 score was selected as the optimal setting to balance

model accuracy and generalization. The final configuration determined was n_estimators = 200, max_depth = 10, min_samples_split = 2, min_samples_leaf = 2. Under this setting, the model achieved excellent performance on the training set (R^2 = 0.94, *RMSE* = 0.68, *MAE* = 0.50), while still maintaining robust performance on the testing set (R^2 = 0.71, *RMSE* = 1.84, *MAE* = 1.25). Further results from five-fold cross-validation (R^2 = 0.71 ± 0.05, *RMSE* = 1.60 ± 0.19) confirmed that the model achieved a favorable balance between fitting accuracy and generalization capability.

Section S3. Surface NO_2 over TP

Using ground-based observations from the CNEMC network during 2015-2024 at major cities across TP, we systematically analyzed the spatiotemporal characteristics of surface NO_2 concentrations. The corresponding results are presented in Fig. S7. The dataset covers most major urban areas across the TP, and we selected 12 populous cities for analysis, with the data subjected to rigorous missing-value filtering and seasonal anomaly screening to ensure temporal continuity and representativeness. Results show that surface NO_2 concentrations across Tibet generally exhibit a distinct seasonal pattern of higher levels in winter and lower levels in summer, with winter monthly means being typically a few times higher than those in summer. This seasonal contrast is particularly pronounced in densely populated cities such as Lhasa and Qamdo. In contrast, the long-term tendencies of surface and column NO_2 diverge: satellite-derived column NO_2 shows an increasing trend, while surface measurements decline, highlighting a discrepancy between columnar loading and near-surface concentrations.

Trend analysis indicates that, except for Shannan where the data were unstable and thus excluded, the remaining cities all exhibit significant negative trends ($p < 0.01$), with the most pronounced decline observed in Tibet. Qamdo shows the strongest annual decrease of –6.28 ± 0.66 % yr^{-1}, while the decline in Lhasa is relatively moderate at –4.17 ± 0.55 % yr^{-1}. Conversely, Aba Prefecture shows a slight upward trend of –1.87 ± 0.78 % yr^{-1}. Among all cities, Lhasa exhibits the largest seasonal amplitude, with winter surface NO_2 concentrations more than twice those in summer; in contrast, Nyingchi and Guoluo show the smallest seasonal difference. The onset of the decreasing trends is not fully synchronized across cities: for example, Qamdo experienced a sustained decline after 2015, whereas Shannan did not show a clear negative trend until after 2022. These discrepancies are likely related to differences in the timing of local energy structure adjustments and the implementation of vehicle emission control policies (Wu et al., 2017; Liu et al., 2023; Abdelwahab et al., 2024).

Section S4. Spatiotemporal patterns of NO_2 variability

Based on the analysis of OMI satellite data from 2005 to 2024, the tropospheric NO_2 vertical column density (VCD) over Tibet and its surrounding regions exhibits pronounced spatial heterogeneity, with the spatial patterns depicted in Fig. 1 and Fig. S8. The 20-year mean NO_2 VCD over the TP is 6.47×10^{15} molec cm^{-2}, significantly lower than that over major South Asian countries such as India and Nepal, reflecting the relatively clean atmospheric background of the TP. However, intra-TP gradients are also evident. The 20-year mean NO_2 VCD values for the seven prefecture-level cities within Tibet are as follows: Ngari, 5.73×10^{15} molec cm^{-2}; Lhasa, 7.23×10^{15} molec cm^{-2}; Nagqu, 5.81×10^{15} molec cm^{-2}; Nyingchi, 7.94×10^{15} molec cm^{-2}; Shigatse, 6.53×10^{15} molec cm^{-2}; Shannan, 1.03×10^{15} molec cm^{-2}; and Qamdo, 5.57×10^{15}

molec cm^{-2}. Among these, relatively high NO_2 VCDs are observed in southeastern regions such as Nyingchi and Lhasa, which may be influenced by pollution accumulation or regional transport processes facilitated by topographic channels. Previous studies have confirmed that pollutants such as CO and HCHO in this region are strongly affected by transboundary transport from northeastern India (e.g., Assam) (Sun et al., 2021; Lin et al., 2024; Xu et al., 2024), and NO_2, as a chemically related species, is likely to be transported together, exhibiting similar spatial patterns.

The temporal trend analysis indicates a coherent seasonal cycle of NO_2 across the TP. Most regions display a characteristic pattern with minima in winter and maxima in summer, controlled by the intensity of photochemical reactions and the development of the planetary boundary layer. A linear regression applied to deseasonalized monthly NO_2 VCD series yields correlation coefficients (R) ranging from 0.65 to 0.94, suggesting that the trend signal is both statistically significant and robust. All subregions exhibit increasing NO_2 concentrations over 2005-2024. The TP-wide mean growth rate is 2.79 ± 0.14 % yr^{-1}, with regional trends spanning from 1.47 ± 0.16 % yr^{-1} in Shannan to 3.41 ± 0.21 % yr^{-1} in Qamdo, highlighting a clear east–west contrast in the pace of enhancement.

However, OMI detected anomalously elevated NO_2 values during the summers of 2023 and 2024. To assess whether these deviations reflect actual atmospheric changes or potential sensor-related issues, we compared the corresponding OMI pixels with matched TROPOMI observations, with the relevant results shown in Fig. S9. The OMI–TROPOMI difference maps indicate that, relative to 2022, the proportion of pixels exhibiting positive biases increased substantially in 2023 and 2024, suggesting that the summertime NO_2 enhancement is unlikely to be driven entirely by physical processes and is more likely to be partly influenced by the gradual decline in OMI performance. This phenomenon is consistent in direction with recent assessments reporting possible sensor aging. Although OMI has been in service for nearly two decades and has experienced a certain degree of performance degradation, its long-term continuous record remains irreplaceable for investigating regional-scale trends and multi-decadal atmospheric changes. Moreover, a discrepancy exists between surface and column concentrations, likely reflecting the differing contributions of boundary-layer processes, regional transport, and emission structures (Zhang et al., 2025a; Zhang et al., 2025b). It is worth noting that previous studies have reported a rapid increase in local NOx emissions in high-altitude cities in recent years, which has also, to some extent, contributed to the divergent changes between surface and column NO_2 concentrations (Xu et al., 2025). CO shows a similar pattern, but with a smaller divergence (see Figs. S10 and S11).

Figures

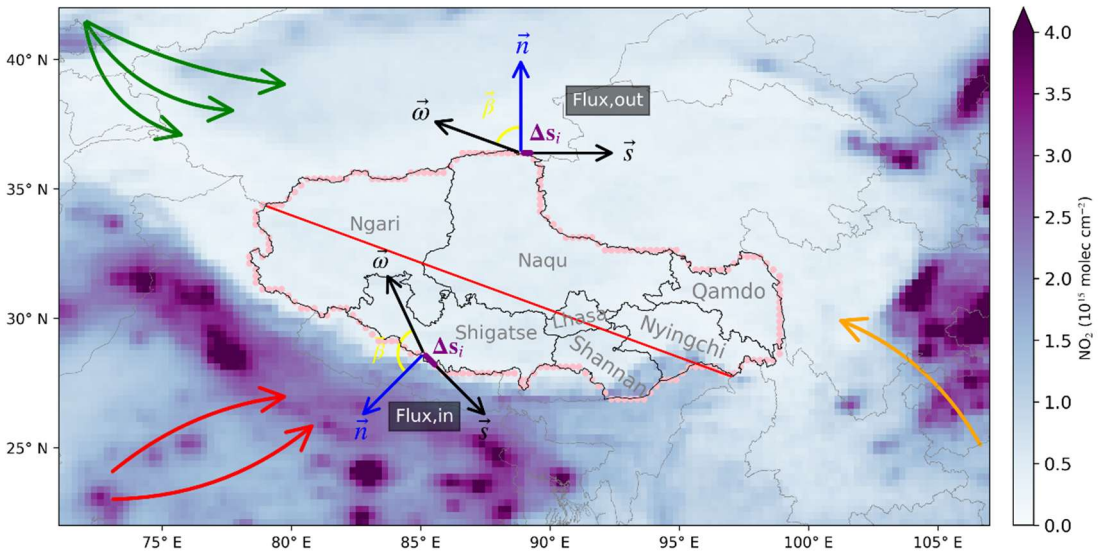

Fig. S1. Illustration of the closed-loop integral method for NO_2 flux calculation. Pink points indicate the closed loop. The black arrow $\boldsymbol{\omega}$ denotes the wind field vector, $\boldsymbol{s}$ is the integration step vector, and the blue arrow $\boldsymbol{n}$ shows the boundary normal vector. β is the angle between $\boldsymbol{\omega}$ and $\boldsymbol{n}$, while Δs represents the integration step length. Green arrows indicate the westerly circulation over the plateau, red arrows denote the South Asian monsoon, and orange arrows show the East Asian monsoon.

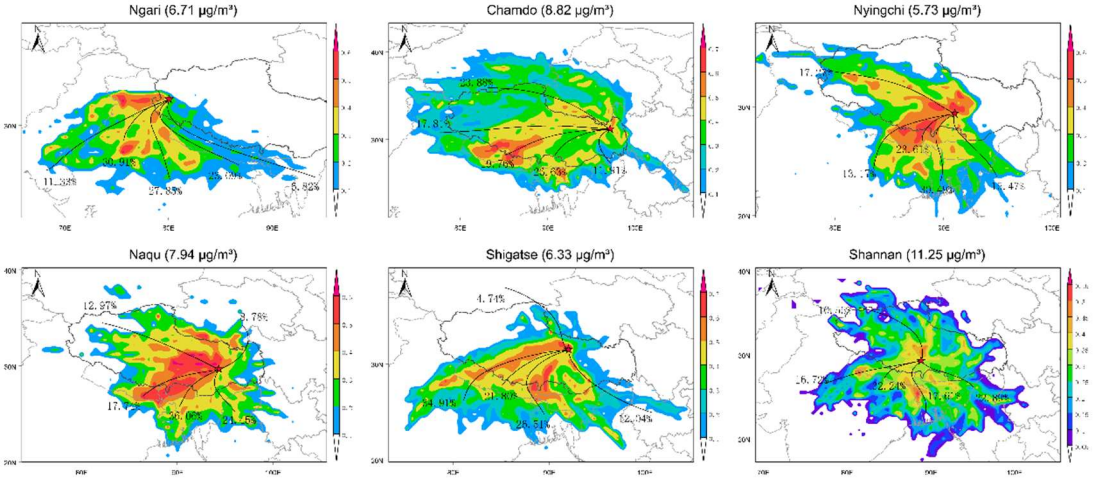

Fig. S2. PSCF-derived potential source regions and clustered back trajectories for TP, categorized into the monsoon periods.

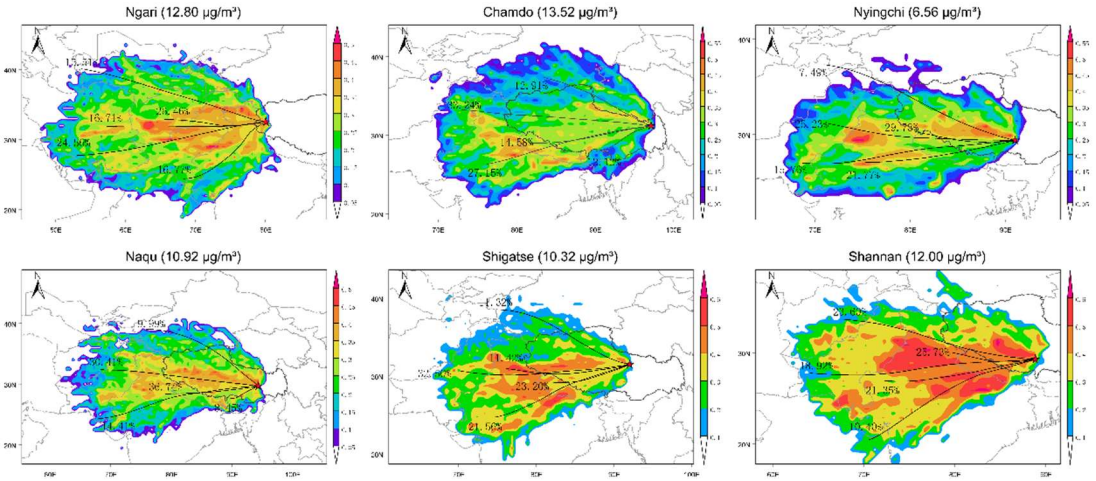

Fig. S3. PSCF-derived potential source regions and clustered back trajectories for TP, categorized into the westerly periods.

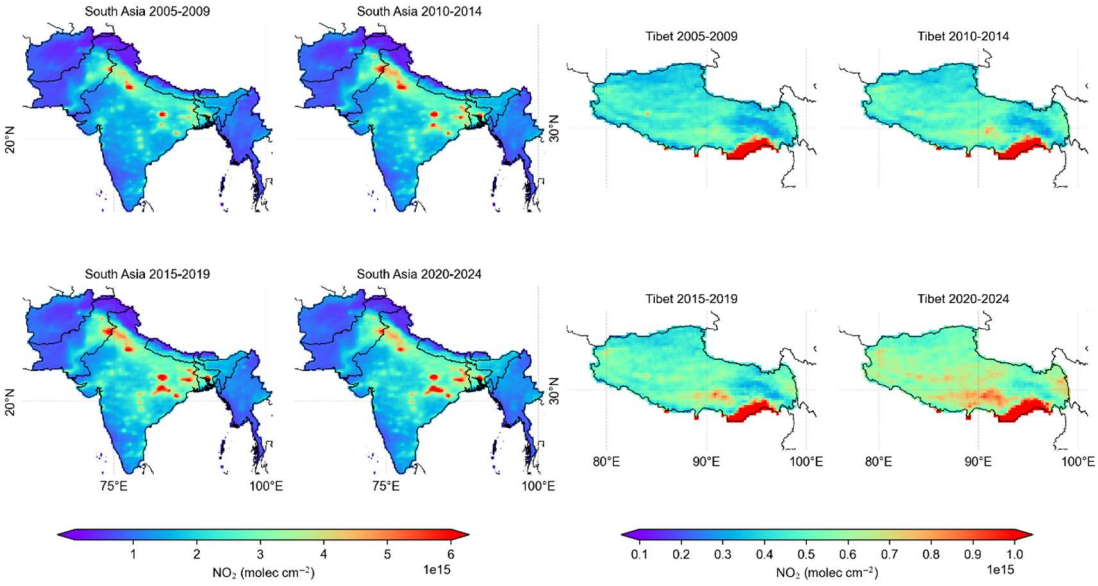

Fig. S4. Five-year grouped changes in NO_2 column concentrations over South Asia and the TP from 2005 to 2024.

Fig. S5. Annual NO_x emissions by sector (energy, transport, agriculture, and industry) across Bangladesh, Delhi, Punjab (Pakistan), and Tibet, derived from EDGAR and aggregated over all pixels within administrative boundaries.

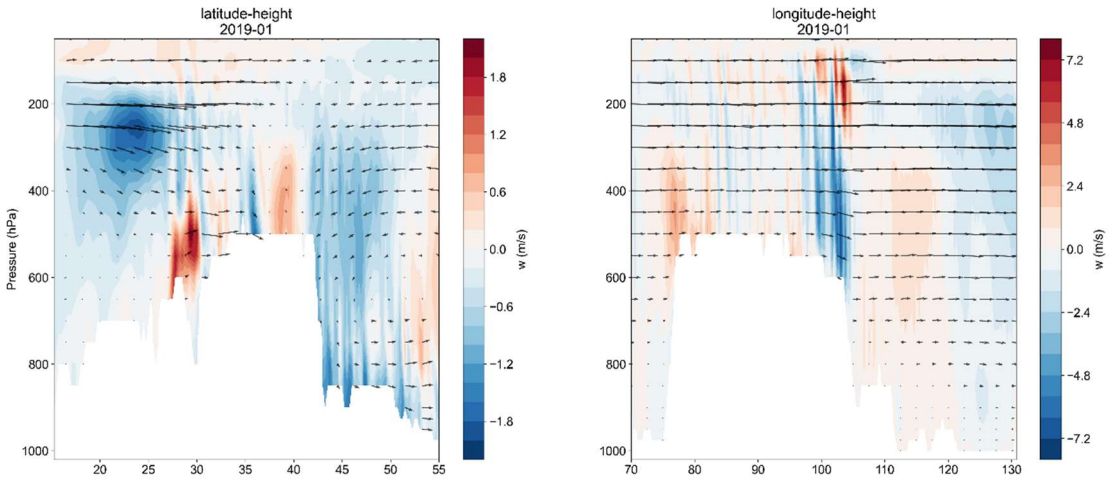

Fig. S6. Vertical Mixing over the Plateau Derived from ERA5 Reanalysis.

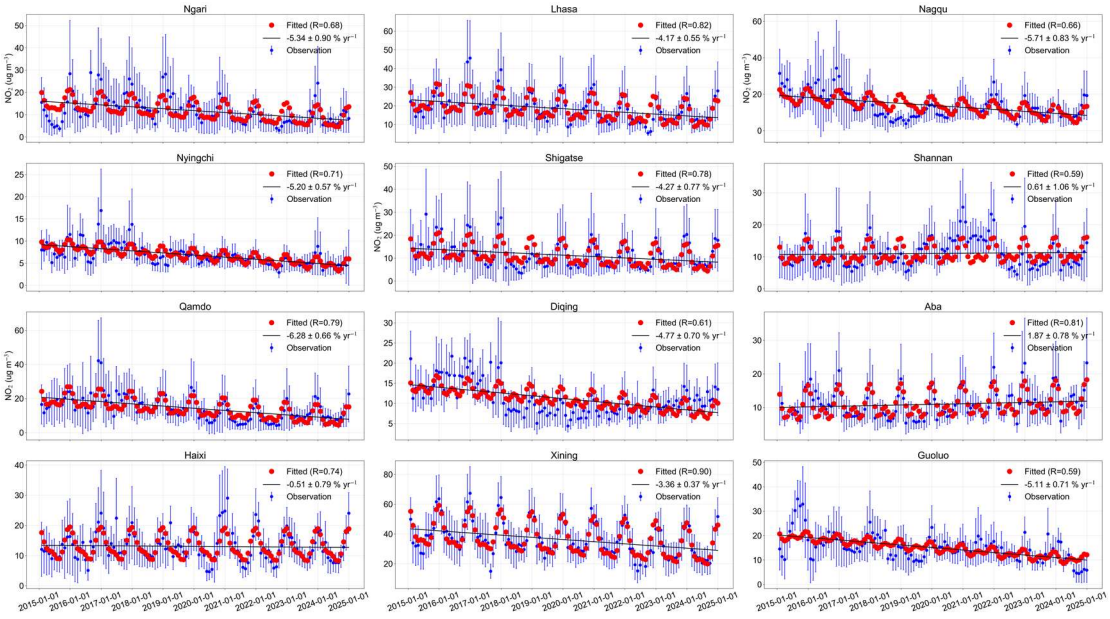

Fig. S7. Temporal evolution of NO_2 concentrations observed by CNEMC from 2015 to 2024. Monthly means (blue) with ±1σ variability are shown alongside the fitted seasonal (red) and long-term (black) components.

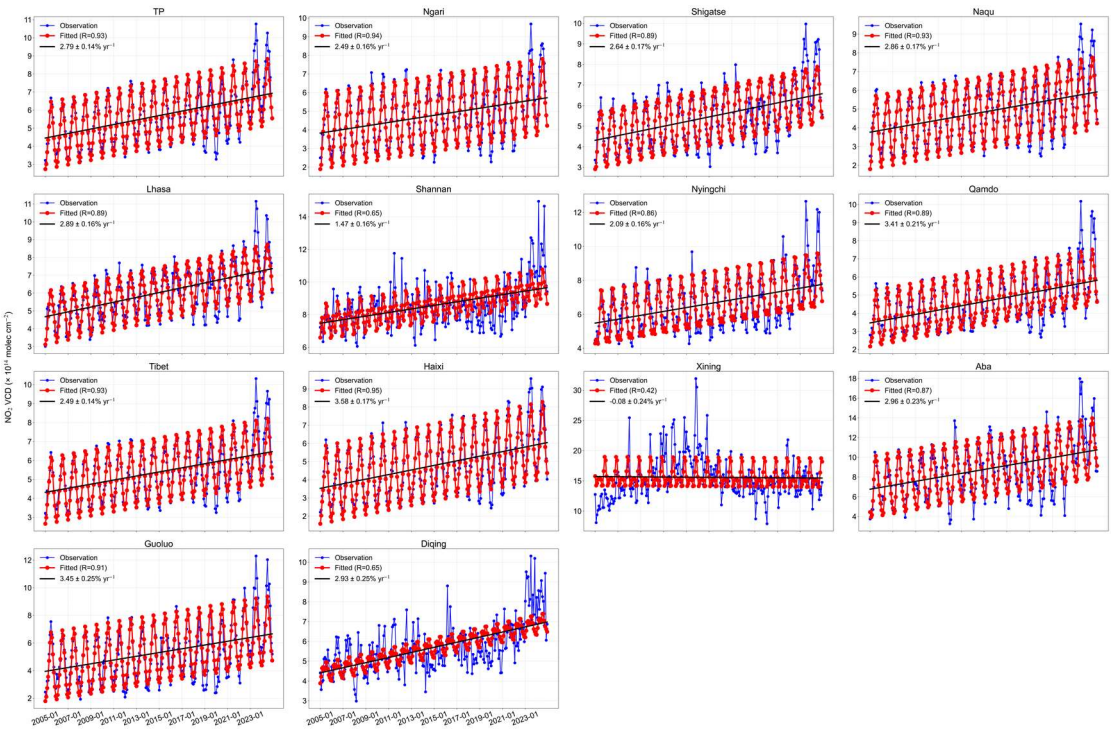

Fig. S8. Long-term NO_2 VCD (2005–2024) over the TP and selected prefecture-level cities, averaged across all pixels within each administrative boundary. Blue dots show monthly mean concentrations, red curves indicate fitted seasonal cycles, and black curves represent interannual trends.

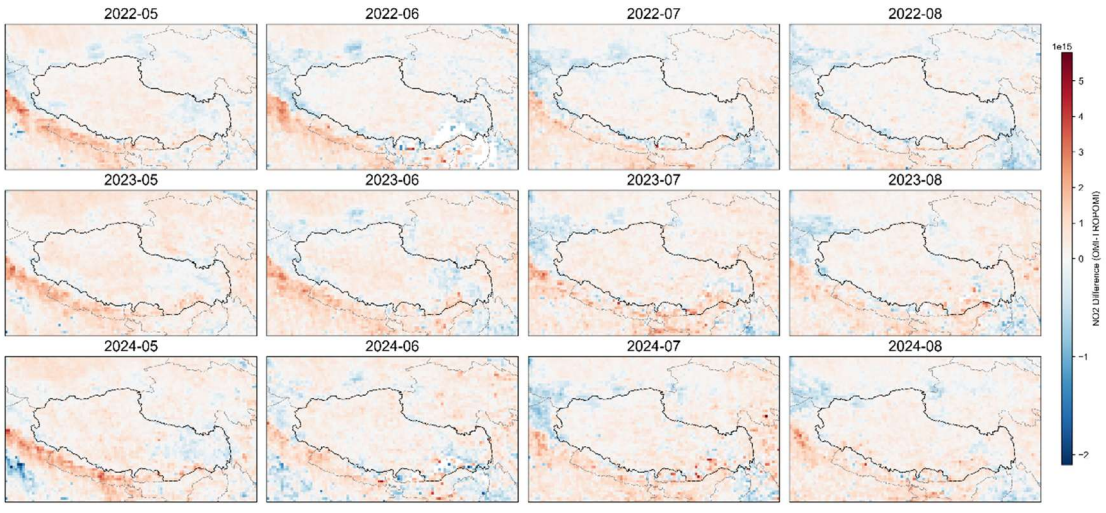

Fig. S9. Pixel-wise differences between OMI and TROPOMI during April–September, 2022–2024

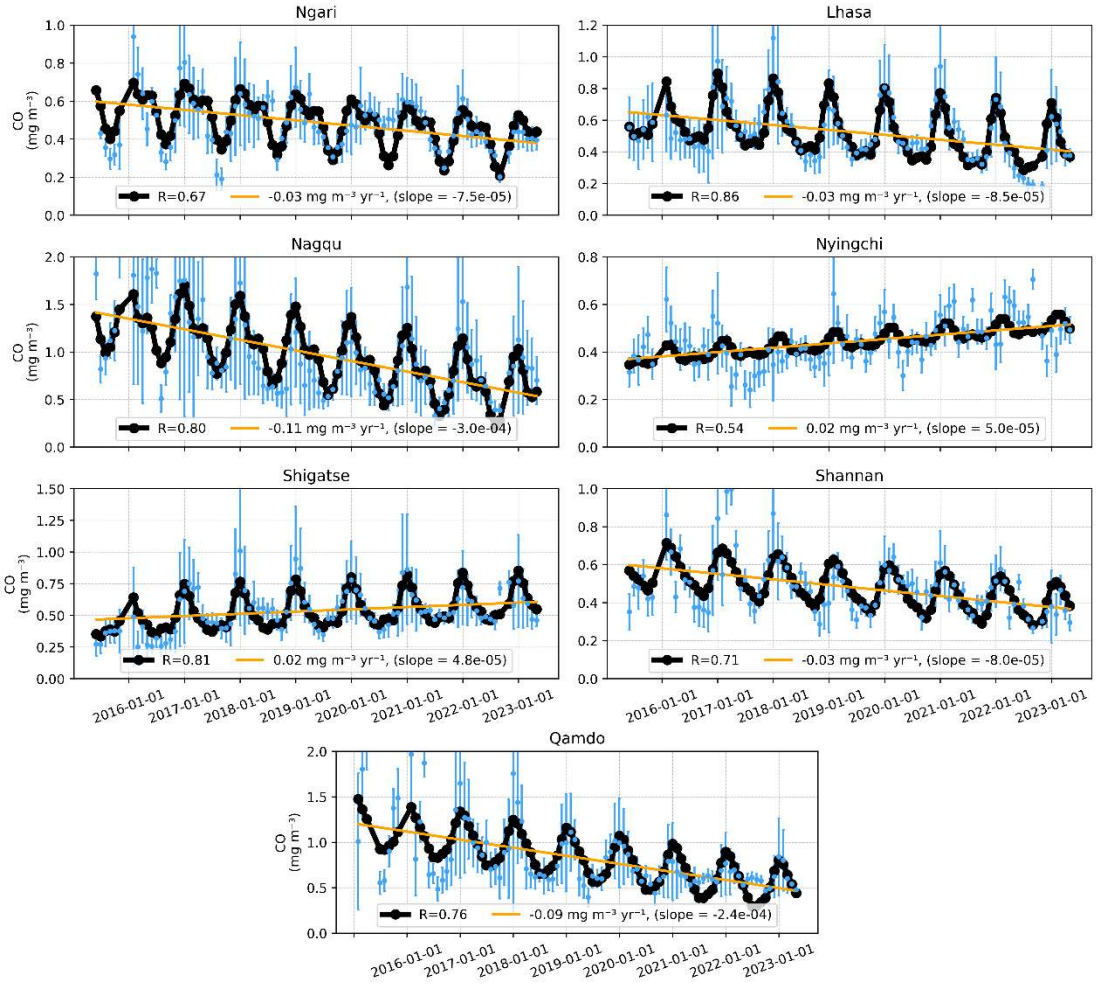

Fig. S10. Inter-annual variations of CO observed by CNEMC from 2015 to 2024. Blue dots represent the monthly mean CO concentration, with vertical error bars indicating the 1σ standard deviation. The seasonal trend (black line) and inter-annual trend (orange line) are fitted using a seasonal cycle model.

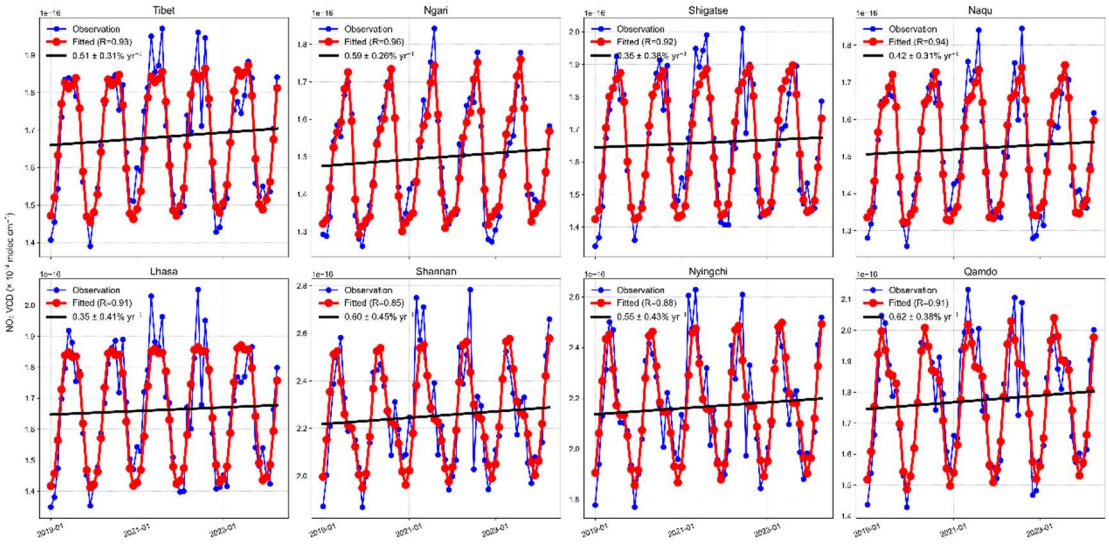

Fig. S11. Long-term fitted CO column concentrations (2019-2024) across the TP and seven representative prefecture-level cities, averaged over all pixels within their administrative boundaries.

Tables

Table S1. Tuned hyperparameters used in the Random Forest model.

Parameter	Description	Tuning range / Selected value
n_estimators	Number of trees in the ensemble	200, 300, 400
max_depth	Maximum depth of each tree	5, 7, 10
min_samples_split	Minimum number of samples required to split an internal node	2, 5, 10
min_samples_leaf	Minimum samples required at a leaf node	1, 2, 4
max_features	Number of features considered when searching for the best split	"None", "sqrt", "log2"
cv folds	Cross-validation folds used in GridSearchCV	5
scoring metric	Metric used for model optimization	R^2

Table S2. Uncertainties in mean wind speed and wind direction after wind-field correction for NO_2 transport flux.

Year	Averaged Wind Speed Uncertainty (m/s)				Averaged Wind Direction and Its Uncertainty (°)			
	MAM	JJA	SON	DJF	MAM	JJA	SON	DJF
2005	3.58	2.13	3.15	4.85	21.01	36.06	14.48	16.01
2006	3.46	1.95	2.77	4.74	16.77	39.58	14.57	15.79
2007	3.23	2.14	3.00	4.64	21.62	40.00	14.47	16.23
2008	3.50	2.10	3.27	5.03	19.84	41.35	13.92	15.59
2009	3.81	2.13	3.32	4.86	23.96	31.27	13.19	15.20
2010	3.71	2.02	3.32	4.59	16.48	38.61	15.54	16.16
2011	3.54	1.99	2.99	5.24	19.80	39.56	14.62	15.90
2012	3.88	2.16	3.26	5.37	20.87	38.70	13.74	16.23
2013	3.34	1.98	3.02	4.85	22.15	39.98	16.04	16.45
2014	3.66	2.08	3.08	5.37	19.22	36.77	12.68	16.41
2015	3.46	2.08	3.10	4.13	16.04	38.24	12.66	16.57
2016	3.38	2.04	3.25	4.82	13.74	33.90	14.58	15.54
2017	3.71	1.99	3.15	4.86	20.74	39.77	12.70	15.95
2018	3.11	1.99	3.11	4.96	15.86	42.05	12.76	15.31
2019	3.89	2.19	3.26	4.15	17.50	35.16	15.36	16.62
2020	3.32	2.19	3.35	4.69	20.01	35.58	12.77	17.45
2021	3.76	2.18	3.30	4.75	18.03	35.48	14.20	15.55
2022	3.32	1.84	3.08	4.77	18.80	35.98	14.48	17.23
2023	3.38	2.03	2.73	4.70	14.77	36.49	12.39	15.48
2024	3.40	2.28	2.89	4.75	20.16	38.30	15.21	15.60

References

Abdelwahab, M. M., Shalaby, O. A., Semary, H. E., and Abonazel, M. R.: Driving Factors of NOx Emissions in China: Insights from Spatial Regression Analysis, Atmosphere, 15, 10.3390/atmos15070793, 2024.

Lin, P., Tian, Y., Borsdorff, T., Li, Z., Landgraf, J., Wu, H., Xue, J., Ding, D., Ye, H., Zhu, Y., and Liu, C.: TROPOMI unravels transboundary transport pathways of atmospheric carbon monoxide in Tibetan Plateau, Sci Total Environ, 952, 175942, 10.1016/j.scitotenv.2024.175942, 2024.

Liu, X. Y., Xu, L. X., Wu, X. Q., and Wen, H. X.: Can China's vehicular emissions regulation reduce air pollution?-a quasi-natural experiment based on the latest National Vehicular Emissions Standard (stage-VI), Environ Sci Pollut Res Int, 30, 112474-112489, 10.1007/s11356-023-30105-7, 2023.

Sun, Y., Yin, H., Cheng, Y., Zhang, Q., Zheng, B., Notholt, J., Lu, X., Liu, C., Tian, Y., and Liu, J.: Quantifying variability, source, and transport of CO in the urban areas over the Himalayas and Tibetan Plateau, Atmos. Chem. Phys., 21, 9201-9222, 10.5194/acp-21-9201-2021, 2021.

Wu, Y., Zhang, S., Hao, J., Liu, H., Wu, X., Hu, J., Walsh, M. P., Wallington, T. J., Zhang, K. M., and Stevanovic, S.: On-road vehicle emissions and their control in China: A review and outlook, Sci Total Environ, 574, 332-349, 10.1016/j.scitotenv.2016.09.040, 2017.

Xu, C., Lin, J., Kong, H., Jin, J., Chen, L., and Xu, X.: Rapid increases in ozone concentrations over the Tibetan Plateau caused by local and non-local factors, Atmos. Chem. Phys., 25, 9545-9560, 10.5194/acp-25-9545-2025, 2025.

Xu, Y., Su, W., Hu, Q., Zhang, C., Javed, Z., Tian, Y., Hou, H., and Liu, C.: Unexpected HCHO transnational transport: influence on the temporal and spatial distribution of HCHO in Tibet from 2013 to 2021 based on satellite, npj Clim. Atmos. Sci., 7, 10.1038/s41612-024-00639-9, 2024.

Yin, H., Sun, Y. W., Notholt, J., Palm, M., Ye, C. X., and Liu, C.: Quantifying the drivers of surface ozone anomalies in the urban areas over the Qinghai-Tibet Plateau, Atmos. Chem. Phys., 22, 14401-14419, 10.5194/acp-22-14401-2022, 2022.

Zhang, X., Ye, C., Kim, J., Lee, H., Park, J., Jung, Y., Hong, H., Fu, W., Li, X., Chen, Y., Wu, X., Li, Y., Li, J., Zhang, P., Yan, Z., Zhang, J., Liu, S., and Zhu, L.: Tropospheric NO2 Column over Tibet Plateau According to Geostationary Environment Monitoring Spectrometer: Spatial, Seasonal, and Diurnal Variations, Remote Sens., 17, 10.3390/rs17101690, 2025a.

Zhang, Y., Wei, Y., de Leeuw, G., Liu, O., Chen, Y., Lv, Y., Zhang, Y., and Li, Z.: Relation between total vertical column density and near-surface NO2 based on in situ and Pandora ground-based remote sensing observations, Atmos. Chem. Phys., 25, 10643-10660, 10.5194/acp-25-10643-2025, 2025b.